

Spin-resolved microscopy of ^{87}Sr $\text{SU}(N)$ Fermi-Hubbard systems

Carlos Gas-Ferrer,^{1,*} Antonio Rubio-Abadal,^{1,†} Sandra Buob,¹
Leonardo Bezzo,¹ Jonatan Höschele,¹ and Leticia Tarruell^{1,2,‡}

¹*ICFO - Institut de Ciències Fotoniques, The Barcelona Institute of Science and Technology, 08860 Castelldefels (Barcelona), Spain*

²*ICREA, Pg. Lluís Companys 23, 08010 Barcelona, Spain*

(Dated: March 6, 2026)

Quantum-gas microscopes provide direct access to the phases of the Hubbard model, bringing microscopic insight into the complex competition between interactions, $\text{SU}(2)$ magnetism, and doping. Alkaline-earth(-like) fermions extend this spin-1/2 paradigm by realizing higher symmetries and giving access to $\text{SU}(N)$ Hubbard models, with rich phase diagrams to be unveiled. Despite its fundamental interest, a microscopic exploration of $\text{SU}(N)$ quantum systems has remained elusive. Here we report the realization of a quantum-gas microscope for fermionic ^{87}Sr . Our imaging scheme, based on cooling and fluorescence on the narrow intercombination line at 689 nm, enables spin-resolved single-atom detection. By implementing a spin-selective optical pumping protocol, we determine the occupation of each of the 10 spin states in a single experimental realization, a crucial capability for probing site-resolved magnetic correlations. We benchmark our method by observing single-particle Larmor precession across the full spin-9/2 ground-state manifold. These results establish ^{87}Sr quantum-gas microscopy as a powerful approach to study exotic magnetism in the $\text{SU}(N)$ Fermi-Hubbard model, and provide a new detection tool for studies in quantum simulation, computation, and metrology.

I. INTRODUCTION

Spin degrees of freedom are fundamental to quantum science, serving as resources for information processing, building blocks of quantum magnetism, and sensitive tools in quantum metrology. In neutral-atom platforms, microscopic control of individual spins has significantly pushed the boundaries of quantum simulation [1, 2]. Quantum-gas microscopes, for instance, have used two-component ground-state mixtures to investigate quantum magnetism in the Fermi-Hubbard [3–5] and isotropic Heisenberg models [6, 7]. Another example is optical-tweezer arrays, which exploit Rydberg-mediated interactions between electronic states to realize quantum Ising [8, 9] and XY models [10], among others. A key aspect of both platforms is the detection of individual atoms, which often cannot resolve spin states in a single experimental realization. Instead, experiments frequently extract spin information indirectly, for example by interpreting the loss of a particular state as an indicator. One popular approach to retrieve the full spin information relies on spin-to-position mapping techniques, either with magnetic-field gradients [5, 11, 12] or state-dependent potentials [13, 14].

So far, microscopic studies of Hubbard and quantum spin models have mostly focused on spin-1/2 systems. The realization and detection of spin models with more

components face several challenges. The first one is the single-atom detection of the different spin states, since methods based on spin separation are hard to scale to atoms with larger spin. The second challenge is the stability of the spin populations in multicomponent mixtures, which are commonly subjected to spin-exchange collisions. Such collisions lead to rich spin dynamics, investigated for various species in optical lattices [15–18], but usually lead to leakage from the original spin populations. An exception for alkali atoms is ^6Li , for which spin-exchange collision rates can remain small in certain regimes [19, 20], as shown in the recent realization of a 3-component Hubbard model [21].

Alkaline-earth(-like) atoms overcome these limitations thanks to their fermionic isotopes with large nuclear spin I , which provide unique opportunities arising from their distinctive internal structure. Firstly, they support narrow and ultranarrow optical transitions, which can be used to individually address the spin states within the ground-state manifold. These transitions have made them the leading choices for quantum metrology with optical atomic clocks [22]. Furthermore, they are strong candidates for neutral-atom quantum computing [23–28], supporting novel paradigms such as fermionic [29, 30] and qudit [31, 32] quantum processing. Secondly, their 2-electron singlet ground state effectively decouples the nuclear spin from the electronic angular momentum. This leads to an $\text{SU}(N)$ interaction symmetry, with the N spin states interacting with identical strength [33, 34]. As a result, collisional spin relaxation processes are suppressed [35]. These properties open the door to the study of exotic models of quantum magnetism. In particular, several theoretical studies have explored the $\text{SU}(N)$ Heisenberg model [36–41], identifying a rich variety of

* C.G. and A.R. contributed equally to this work

† Present address: Departament de Física Quàntica i Astrofísica, Facultat de Física, Universitat de Barcelona, 08028 Barcelona, Spain

‡ leticia.tarruell@icfo.eu

magnetic phases of matter. These include phases with spontaneous dimerization [38], plaquette order [40], and chiral spin liquids for large N [36]. Recent works have also focused on models with itinerance, leading to an even richer phenomenology emerging from the competition between motion and magnetism. For example, zig-zag antiferromagnets and alternating long-range order have been found near the ground state of the SU(3) Fermi-Hubbard model [42–44], and the emergence of magnetic polarons was investigated in the doped SU(3) t - J model [45].

To date, ultracold SU(N) fermions with large N have been experimentally realized mostly with ^{173}Yb ($I = 5/2$ with $N = 6$) [46] and ^{87}Sr ($I = 9/2$ with $N = 10$) [47]. Experiments with bulk SU(N) gases have explored systems with different dimensionalities and studied aspects such as their spectroscopic response [48], the emergence of bosonization for large N [49, 50], or their thermodynamical properties [51]. By loading the clouds into three-dimensional optical lattices, the SU(N) Fermi-Hubbard model has been realized [52]. It has allowed the implementation of synthetic gauge fields using the nuclear spin states of the ground-state manifold as a synthetic dimension [53, 54], the measurement of the equation of state of the system across the Mott crossover [55, 56], and the observation of flavor-selective localization when breaking the SU(N) symmetry [57]. An exciting frontier for these systems is the detection of SU(N) quantum magnetism. Recently, first signals of nearest-neighbour correlations have been observed in an SU(6) Hubbard system using ^{173}Yb [58]. However, all experimental studies so far have relied exclusively on global measurements, since alkaline-earth(-like) quantum-gas microscopes have only been realized with bosonic isotopes [59–61]. Given that microscopic observables have been key to reaching low entropies [62] and detecting long-range magnetism [63] in the SU(2) Hubbard model, an SU(N) Fermi-gas microscope is highly desirable to unveil the exotic SU(N) quantum magnetic phases.

In this work, we demonstrate quantum-gas microscopy of a fermionic alkaline-earth species, ^{87}Sr . The backbone of our system is the narrow intercombination line, which we use for both cooling and imaging, similarly to recent works with fermionic ^{171}Yb and bosonic ^{88}Sr in optical tweezers [25, 28, 64]. Furthermore, we introduce spin-resolved optical pumping and demonstrate an imaging protocol which enables the sequential and independent site-resolved detection of all 10 spin states of strontium in a single experimental run. This capability will enable the direct measurement of spin-spin correlations in SU(N) Fermi-Hubbard systems with $N \leq 10$. Our imaging protocol could be applied to other atomic species featuring narrow-linewidth transitions and offers a versatile detection method for quantum computing schemes based on the nuclear spin of ^{87}Sr [29, 31].

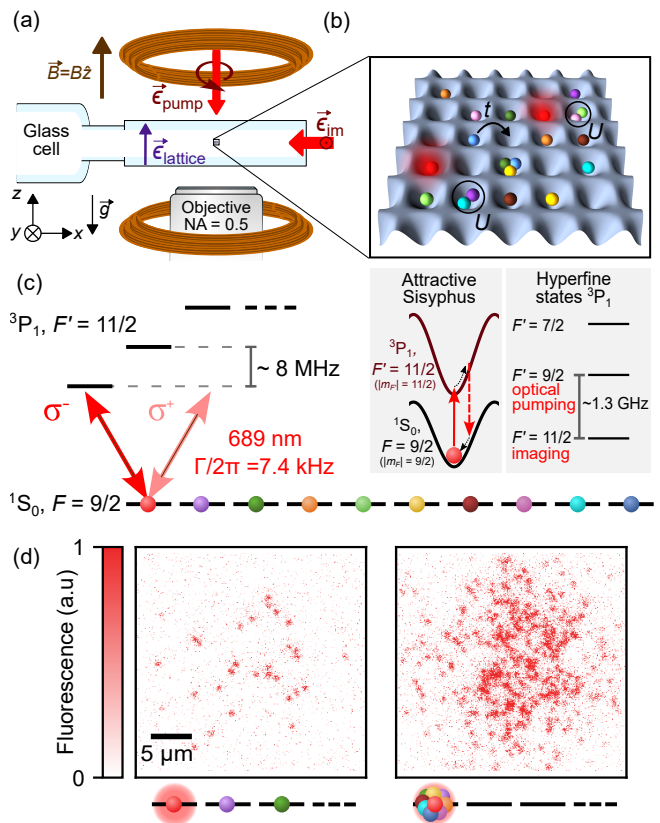


FIG. 1. Microscopy of fermionic ^{87}Sr atoms in an optical lattice. (a) Side-view schematic of the setup. Atoms are trapped in a square optical lattice at the center of a glass cell. A coil pair produces a vertical magnetic field \vec{B} aligned with the lattice polarization, $\vec{\epsilon}_{\text{lattice}}$. A 689 nm imaging beam enters horizontally with linear polarization, and scattered light is collected by a 0.5-NA objective. A circularly polarized optical-pumping beam is sent vertically. (b) Schematic of an SU(10) Fermi-Hubbard system with tunneling rate t and on-site interaction energy U . Only $m_F = -9/2$ (red) atoms are addressed by the imaging light. (c) Energy level diagram of the ground and excited $^3\text{P}_1$ $F' = 11/2$ state, showing the splitting of their Zeeman sublevels. The imaging light has σ^+ and σ^- components but only resonantly addresses the $^1\text{S}_0 |F = 9/2, m_F = -9/2\rangle \rightarrow ^3\text{P}_1 |F' = 11/2, m_{F'} = -11/2\rangle$ transition, which satisfies the condition for attractive Sisyphus cooling (inset, left panel). Two different transitions within the hyperfine structure of the $^3\text{P}_1$ manifold are used for optical pumping and imaging (inset, right panel). (d) Consecutive fluorescence images of a thermal cloud with 300 atoms. Left image: atoms in state $m_F = -9/2$. Right image: atoms in all states taken after a set optical pumping pulses, showing a ten-fold increase in atom number.

II. EXPERIMENTAL SETUP AND NARROW-LINE IMAGING

In our experiment, we routinely prepare cold atomic clouds of ^{87}Sr in the center of an ultra-high-vacuum glass cell, sketched in Fig. 1(a). Such a cloud is, by default, spin-unpolarized, with all 10 Zeeman sublevels of the

ground state 1S_0 $F = 9/2$ equally populated. This results from the standard laser-cooling stages used of ^{87}Sr , which require an additional “stirring” laser for spin mixing during narrow-line cooling [65]. After laser cooling, the atomic cloud is loaded into a 1064 nm optical dipole trap and then transferred to the optical lattice potential. It consists of a four-fold interfering square lattice with 575 nm spacing and a vertically confining light sheet; both operating at $\lambda = 813.4$ nm. This clock-magic wavelength for strontium ensures that both the ground 1S_0 and excited clock 3P_0 states are equally trapped. Further details of the cooling process and trapping potentials can be found in App. A and in our previous work with bosonic strontium [61].

The resulting system realizes the two-dimensional $SU(N)$ Fermi-Hubbard model, with N (up to 10) controlled by the number of populated Zeeman sublevels. A schematic picture of this model is shown in Fig. 1(b). In order to access the microscopic occupation of the system, the depth of the optical lattice is strongly increased to pin the positions of the atoms to their respective lattice sites, including during the imaging process.

Fluorescence imaging of strontium atoms is typically performed on the broad 461 nm [61, 66–68]. Most experiments combine imaging with simultaneous cooling to increase the number of scattered photons, although fast-exposure methods without cooling have also been recently demonstrated [69]. Cooling is based on the narrow 689 nm intercombination line (linewidth $\Gamma/2\pi = 7.4$ kHz), which has enabled both narrow-line Sisyphus [61, 64, 66, 68, 70] and resolved sideband cooling [66, 67] in optical tweezers and lattices. Exploiting instead fermionic ^{87}Sr considerably complicates the detection process. On the one hand, the hyperfine structure of the blue transition is not resolved, leading to spin mixing. On the other hand, cooling all 10 ground states on the narrow line is challenging due to their differing light shifts. Further details are provided in App. B.

In this work, we overcome these challenges by performing fluorescence imaging of ^{87}Sr directly on the narrow-line transition. This allows scattering of fluorescence photons that simultaneously cool the atoms, as recently demonstrated with bosonic ^{88}Sr in optical tweezer arrays [64]. In ^{87}Sr , the excited 3P_1 $F' = 11/2$ state provides two cycling transitions suitable for attractive Sisyphus cooling: $^1S_0 |F = 9/2, m_F = \pm 9/2\rangle \rightarrow ^3P_1 |F' = 11/2, m_{F'} = \pm 11/2\rangle$. Here F (F') and m_F ($m_{F'}$) denote the total angular momentum and magnetic quantum numbers of the ground(excited) state, respectively.

We exploit the narrow linewidth of the imaging transition to make the imaging process inherently spin-resolved. Our imaging beam resonantly addresses the $^1S_0 |9/2, -9/2\rangle \rightarrow ^3P_1 |11/2, -11/2\rangle$ cycling transition, while all other transitions remain off-resonant, see Figs. 1(b) and (c). We reach this regime by setting a bias magnetic field of $B \approx 20$ G, which results in a Zeeman splitting of the $F' = 11/2$ excited state sublevels

of $\Delta E = g_{F'} m_{F'} \mu_0 B$. Here $g_{F'}$ is the g-factor of the excited state and μ_0 is the vacuum permeability. Combined with the optical light shifts, it yields an overall energy splitting of approximately 8 MHz, which is three orders of magnitude larger than the linewidth of the transition and ensures the independent addressing of a single spin state. Furthermore, the high efficiency of the cooling process makes it possible to work with relatively shallow trapping potentials. Specifically, we set the light sheet and the lattice depths to 55 μK and 80 μK , respectively.

Figure 1(d) shows raw fluorescence images of a thermal cloud, taken with an exposure time of 300 ms and a near-resonant beam of intensity $400 I_{\text{sat}}$, where I_{sat} is the saturation intensity of the transition. During imaging, the atoms are repumped out of the metastable states $^3P_{0,2}$ using lasers at 679 and 707 nm, respectively. The first image (left panel) is spin-resolved and contains approximately 30 detected atoms. Next, we optically pump all atoms into the stretched $^1S_0 |9/2, -9/2\rangle$ state (see App. D for details) and acquire a second image (right panel). We observe roughly a tenfold increase in the number of detected atoms. Averaging over 50 such image pairs, we find an enhanced factor of 9.5(1.2), consistent with an even distribution of the atoms over the 10 spin states.

To characterize the performance of the imaging process, we compare two consecutive pictures of spin-polarized clouds. During the 300 ms exposure, we collect around 100 photons per atom, allowing us to reconstruct their occupation matrices, n^{ref} and n respectively. These matrices contain entries $n_{i,j} = 1$ if the lattice site (i, j) is occupied and 0 otherwise. We extract the pinning fidelity of the imaging process, \mathcal{F}_{pin} , defined as the probability that an atom detected in the first picture is also detected in the second one, by computing the normalized overlap

$$\mathcal{O} = \frac{\langle n, n^{\text{ref}} \rangle}{N_{\text{ref}}} = \frac{\sum_{i,j} n_{i,j} n_{i,j}^{\text{ref}}}{\sum_{i,j} n_{i,j}^{\text{ref}}}, \quad (1)$$

where N_{ref} is the total atom number detected in the first picture. This analysis yields $\mathcal{F}_{\text{pin}} = 92.5(7)\%$, where we identify a hopping rate of $\mathcal{H} = 1.0(3)\%$ and a loss rate of $\mathcal{L} = 6.5(7)\%$ (see App. C for further details). As we discuss in Sec. IV, a large fraction of the detected loss rate \mathcal{L} does not arise from atoms physically leaving the lattice, but rather from spin depolarization processes.

III. SPIN-SELECTIVE MANIPULATION

The presented narrow-line imaging enables the detection of the stretched state, but additional spin manipulation tools are required to measure all other spin states. A common option is optical pumping, which can be used to efficiently transfer atoms through the ground-state manifold. In recent works with optical tweezers [25, 28], a combination of narrow-line imaging and optical pumping was used to retrieve the spin-1/2 populations of fermionic

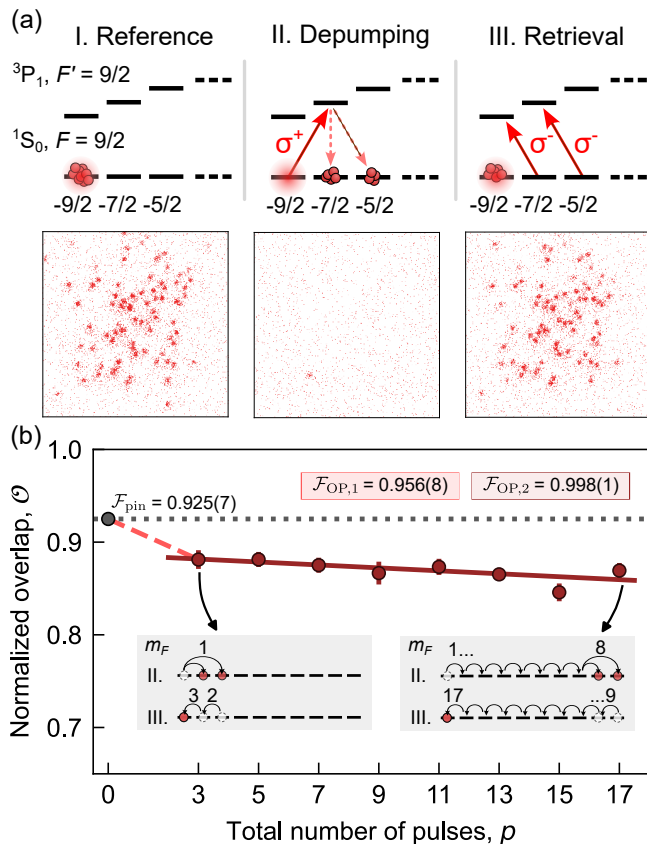


FIG. 2. Narrow-line spin-resolved optical pumping. (a) Procedure to characterize the optical pumping fidelity. Left: a reference picture of a spin-polarized cloud is taken via narrow-line fluorescence, represented with a glowing spot. Center: the population of the initial state is depumped through an optical pumping pulse of σ^+ polarization addressing the $m_{F'} = -7/2$ state. A subsequent image shows practically no atoms, highlighting the spin-resolved nature of the detection. Right: two optical pumping pulses of σ^- polarization retrieve the atomic population back to the $m_F = -9/2$ state and the cloud is imaged again. (b) Optical pumping with an increasing number of pulses p , which bring the atoms to different m_F states and subsequently retrieve them in the stretched $m_F = -9/2$ state (insets). The normalized overlap \mathcal{O} decreases with p (circles) and yields two distinct optical-pumping fidelities $\mathcal{F}_{\text{OP},1}$ and $\mathcal{F}_{\text{OP},2}$ (boxes). $\mathcal{F}_{\text{OP},1}$ is determined by comparing the $p = 3$ value to the pinning fidelity $\mathcal{F}_{\text{pin}} = 92.5(7)\%$ (red dashed and gray dotted lines). $\mathcal{F}_{\text{OP},2}$ is extracted from a linear fit to the data for $p \geq 3$ (dark red solid line).

^{171}Yb atoms. In our case, the 10-state manifold of ^{87}Sr adds significant complexity to the optical pumping scheme compared to a 2-state scenario. Furthermore, detection in quantum-gas microscopes faces additional challenges, such as hopping of the atoms during imaging and manipulation, as well as the requirement of higher fluorescence signal-to-noise ratio in order to resolve the closely spaced sites. In this section, we demonstrate and quantify the performance of spin-resolved optical pumping of ^{87}Sr using its narrow line. In contrast to our imag-

ing scheme, which relies on exciting the $F' = 11/2$ state, we perform optical pumping via the $F' = 9/2$ excited state, which has more favorable coupling properties, see App. D.

To characterize the fidelity of the spin transfer, we analyze the performance of different sequences of optical pumping pulses (see parameters in App. D). We begin by preparing all atoms in the $m_F = -9/2$ state and taking a reference image of their positions. From this reference, we obtain the initial occupation n^{ref} , see left panel of Fig. 2(a). We then apply a $^1S_0 |9/2, -9/2\rangle \rightarrow ^3P_1 |9/2, -7/2\rangle$ optical pumping pulse, selectively depumping the atoms from the stretched state, and acquire a second image showing virtually no fluorescence signal, see central panel. Finally, we transfer the atomic population back to $m_F = -9/2$ state through two successive optical pumping retrieval pulses and image it again, see right panel. We compare the occupation before and after the optical pumping procedure using Eq. (1), which yields the fraction of atoms detected in the first image that returned to the same lattice site in the last one. We obtain a normalized overlap $\mathcal{O} = 88(1)\%$. The value is slightly below the pinning fidelity $\mathcal{F}_{\text{pin}} = 92.5(7)\%$ due to the finite optical pumping fidelity to the stretched state $\mathcal{F}_{\text{OP},1}$. We model it as $\mathcal{O} = \mathcal{F}_{\text{pin}} \mathcal{F}_{\text{OP},1}$, which yields $\mathcal{F}_{\text{OP},1} = 95.6(8)\%$.

The same optical pumping procedure can be performed for an increasing number of depumping and retrieval pulses p . First, a reference image is acquired; the atoms are then depumped into a pair of m_F states in the ground-state manifold; finally they are retrieved to the initial state. An intermediate measurement after depumping confirms that the population remaining in the first $(p-1)/2$ states is negligible, demonstrating the reliability of the depumping. The final retrieval measurement, after pumping the atoms back to the initial state, yields the normalized overlap \mathcal{O} . We plot it as a function of the total number of pulses p in Fig. 2(b). For $p = 5$, \mathcal{O} decreases only slightly compared to $p = 3$, and the overlap shows minimal reduction as p increases further. These results indicate that the optical pumping fidelity for the stretched state, $\mathcal{F}_{\text{OP},1}$, differs appreciably from that for the central states (see App. D). To quantify the overlap decrease for $p \geq 3$, we perform a linear fit to the data. The linear dependence is consistent with a high optical-pumping fidelity $\mathcal{F}_{\text{OP},2}$ between the central states, since the total fidelity can be approximated as $(\mathcal{F}_{\text{OP},2})^p \approx 1 - (1 - \mathcal{F}_{\text{OP},2}) \cdot p$. From the fit, we estimate $\mathcal{F}_{\text{OP},2} = 99.8(1)\%$. Overall, these results indicate that single-atom spin manipulation via optical pumping can be performed with high efficiency, without leading to appreciable losses or hopping.

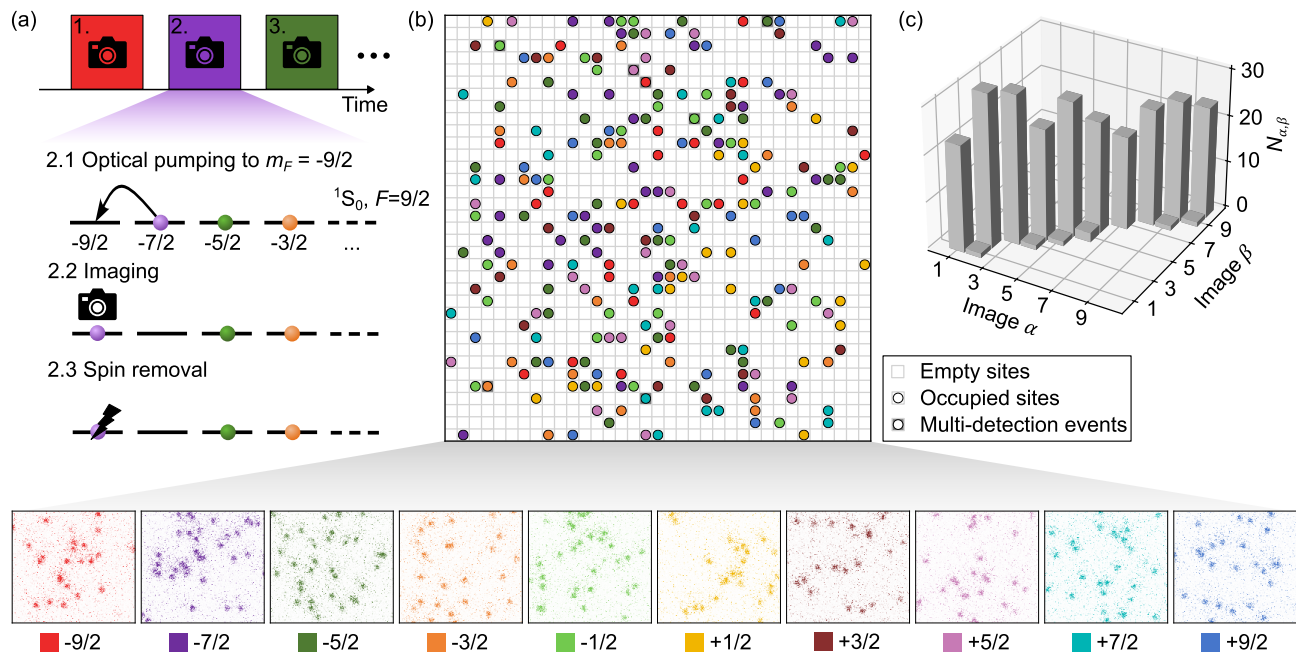


FIG. 3. Spin-resolved microscopy of the 10 states of ^{87}Sr . (a) The imaging protocol consists of 10 detection blocks, one per spin state, carried out sequentially from the $m_F = -9/2$ to the $m_F = +9/2$ state. Each detection block starts by optically pumping the target spin state to the $m_F = -9/2$ state, followed by spin-resolved fluorescence imaging, and concludes with spin-removal of the population to the $m_F = -9/2$ by means of a blue-detuned pulse on the imaging transition. (b) Merging the reconstructed images yields the spin-resolved occupation for all 10 spin states in a single experimental sequence. Below are the 10 raw snapshots, with the colormap indicating the corresponding spin. The images correspond to 35×35 lattice sites containing 253 atoms evenly distributed among the 10 spin states. (c) Image-to-image detection coincidences between the different images, $N_{\alpha,\beta}$. The 10 bars on the diagonal indicate the spin populations. The presence of off-diagonal coincidences corresponds to the multi-detection events, which are indicated with gray shaded squares in (b). They are primarily caused by off-resonant scattering of the trapping light leading to spin depolarization (see main text).

IV. SPIN-RESOLVED DETECTION OF $\text{SU}(10)$ FERMIONS

In the Fermi-Hubbard model, quantum magnetism arises through the superexchange coupling between nearest-neighbour spins. Due to the Pauli exclusion principle, the emerging spin-spin interaction is antiferromagnetic, and leads to anticorrelated spins. $\text{SU}(2)$ antiferromagnetism can be characterized by spin-spin correlators such as $C_{ij}^z = \langle \hat{S}_i^z \hat{S}_j^z \rangle$. These correlators can be probed by accessing the site-resolved spin populations since the spin operator can be expressed as $\hat{S}_i^z = \frac{1}{2}(\hat{n}_i^\uparrow - \hat{n}_i^\downarrow)$, with $\hat{n}_i^{\uparrow(\downarrow)}$ denoting the particle number in state \uparrow (\downarrow) and site i . Quantum-gas microscopes have enabled the measurement of such magnetic correlations by directly measuring \hat{n}_i^σ . However, light-assisted collisions during fluorescence imaging lead to the detection of parity-projected occupation operators [2]. Additionally, spin-resolved detection often relies on spin removal techniques [3, 4], which make it impossible to distinguish holes, doublons, and one of the spins. An independent identification of both spins, needed to measure more advanced correlators [71], requires more complex techniques, such as Stern-Gerlach splitting [5, 11, 12, 21, 72] or polarization-sensitive de-

tection [73, 74].

When dealing with $\text{SU}(N)$ systems with large N , measuring magnetic correlations becomes even more challenging. The relevant spin correlator is

$$C_{ij}^z = \sum_{\sigma \neq \tau} [\langle \hat{n}_i^\sigma \hat{n}_j^\sigma \rangle - \langle \hat{n}_i^\sigma \hat{n}_j^\tau \rangle], \quad (2)$$

which involves the particle number operators \hat{n}_i^σ for each of the N states, with $\sigma, \tau \in \{1, \dots, N\}$. For $N > 2$, extracting C_{ij}^z therefore requires simultaneous single-atom and full-spin resolution, a capability that has not yet been realized. Despite this, recent experiments have made progress towards the microscopic study of multi-component systems. Firstly, the detection of two spin states of ^{87}Sr was achieved in optical tweezers, using the long-lived $^3\text{P}_0$ state to shelve one spin in a dark state while imaging the other [24]. A second experiment achieved fluorescence detection of the occupation of ^{173}Yb atoms in optical tweezers through broad-line imaging [75]. However, this led to mixing of all 6 spin states, i.e., no spin information could be retrieved. Finally, in optical-lattice systems, quantum-gas microscopy of 3 spin states of ^6Li has been realized by removing one of the spins and detecting only the remaining two independently [21].

In this section, we go far beyond these previous experiments by probing the spin-resolved occupation of an SU(10) system. This is achieved by combining the techniques introduced in the preceding sections: spin-resolved imaging of the stretched state and spin-selective optical pumping. As schematically shown in Fig. 3(a), our protocol comprises 10 sequential detection blocks corresponding to the imaging of the 10 ground states. Each block starts with selective optical pumping of the target spin state into $m_F = -9/2$. In a second step, the atoms are imaged by addressing the $^1S_0 |9/2, -9/2\rangle \rightarrow ^3P_1 |11/2, -11/2\rangle$ transition. Finally, the detected atoms are discarded via a spin-removal pulse.

The bottom panel of Fig. 3(b) shows the 10 raw images captured in a single experimental realization, each corresponding to atoms detected in one of the 10 spin states. Reconstructing the occupation from these images yields the spin-resolved occupation matrix, displayed in the central panel of Fig. 3(b), with each spin state represented by a distinct color. From this matrix, we directly access the \hat{n}_i^σ operators for all σ and consequently, the spin-spin correlators. This capability is essential for revealing the magnetic properties of the SU(N) Fermi-Hubbard model [76]. In particular, these measurements provide access to higher-order correlators [71], which are crucial for understanding the many-body character of Hubbard systems.

From our measurements we observe that a few lattice sites, highlighted with a gray background in Fig. 3(b), are occupied in more than one image. This observation is inconsistent with the expected parity projection during fluorescence imaging. We investigate these multi-detection events by computing the overlap between each possible pair of images, α and β , as $N_{\alpha,\beta} = \langle n^\alpha, n^\beta \rangle$. Here, $N_{\alpha,\alpha} = N_\alpha$ is the number of occupied sites in image α , while $N_{\alpha,\beta}$ with $\alpha \neq \beta$ counts the sites that are occupied in both images. The results, shown in Fig. 3(c), reveal non-zero values between subsequent images, with the first off-diagonal terms $N_{\alpha,\alpha+1}$ being the largest contribution. In the specific example of Fig. 3, we measure 7 multi-detection events out of 253 atoms. Averaging over 40 repetitions of the experiment, the total off-diagonal counts correspond to 4.2(4)% of the total atom number, with the first off-diagonal counts contributing 2.8(4)%. This effect cannot be explained by the inefficiency of the spin removal pulse, estimated at < 0.5(2)%, and must be caused by spin depolarization during imaging.

The main mechanism contributing to spin depolarization is trap-induced off-resonant Raman scattering within the excited state manifold (see App. E). As in optical atomic clocks [77], the 813.4 nm light generating the optical lattice and light-sheet potential can drive two-photon off-resonant transitions within the 3P_J manifold. Consequently, atoms in the imaging cycle may abruptly transition to a different state within the triplet manifold. Upon decay or repumping, these atoms can populate ground states with $m_F \neq -9/2$, opening the imaging cycle. This process is the main limitation to the observed pinning

fidelity \mathcal{F}_{pin} and causes the same atom to appear in consecutive images. Overall, these results show that our detection scheme not only is ready to detect SU(N) quantum magnetism but also provides a sensitive diagnostic for identifying spurious processes that could be missed by other imaging methods.

V. COHERENT LARMOR PRECESSION

To benchmark our spin-resolved protocol, we study the Larmor precession dynamics of the ground-state nuclear spin, $F = 9/2$. The experiment is performed in a deep optical lattice, which suppresses hopping and isolates single-particle spin dynamics. A bias magnetic field along the z axis defines the quantization direction, splitting the nuclear Zeeman sublevels of the ground state by $\Delta E = g_I m_F \mu_0 B \approx h \times 184 \text{ Hz/G}$, where $g_I \approx -1.32 \cdot 10^{-4}$ [78, 79] is the nuclear spin g-factor of ^{87}Sr and h is the Planck constant. Following a sudden change in the direction of the quantization axis, the spin undergoes coherent precession with a period $T = h/(g_I \mu_0 B_p)$, where B_p is the magnitude of the magnetic field during the precession. The evolution of the spin is then tracked using our spin-resolved imaging protocol.

Figure 4(a) summarizes our spin-precession experiment. We begin with a spin-polarized cloud of atoms prepared in the $^1S_0 |9/2, -9/2\rangle$ state under a vertical magnetic field of $B_z \simeq 20 \text{ G}$, from which we acquire a reference image of the atomic occupation, n_{ref} . We then rapidly rotate the magnetic field into the horizontal plane, setting it to B_y and initiating Larmor precession. After a variable evolution time t_p , the magnetic field is switched back to B_z , freezing the spin dynamics and allowing us to perform the spin-resolved imaging protocol presented in Sec. IV. Figure 4(b) shows four snapshots of the reconstructed spin occupations at different precession times t_p .

We present the spin-resolved precession dynamics in the top panel of Fig. 4(c). The plot shows the normalized overlap \mathcal{O}_{m_F} for each spin state as a function of the precession time t_p . The results provide clear evidence of nuclear spin coherence over the measured time range, which extends to hundreds of milliseconds. We observe coherent spin oscillations with revivals of the $m_F = -9/2$ state at integer multiples $t_p = nT$, and a maximum population transfer to the $m_F = +9/2$ state at $t_p = (n + 1/2)T$, where $T = 40.16(6) \text{ ms}$. A fit to the oscillations yields a magnetic field of $B_y = 135.0(2) \text{ mG}$. These oscillations provide a stringent benchmark for our imaging protocol, as each evolution time t_p produces a deterministic spin distribution.

In the previous section, we identified spin depolarization as the dominant contribution to the imaging infidelity. To isolate additional sources of infidelity, we extract a spin-insensitive observable from the data shown in Fig. 4(c). Specifically, we combine the occupation ma-

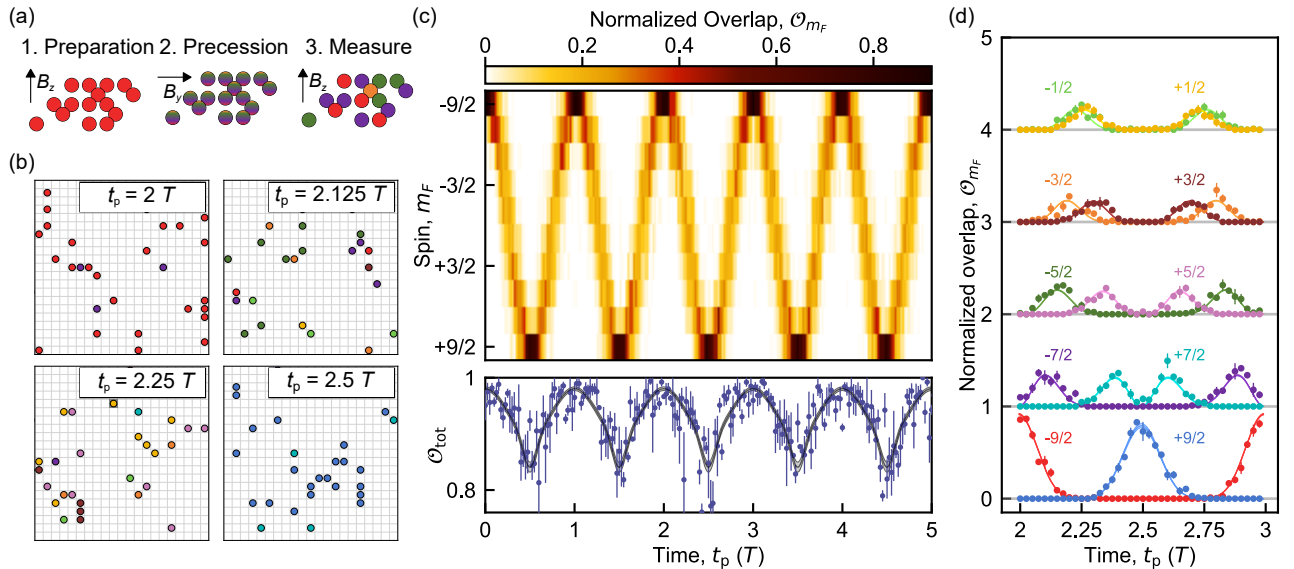


FIG. 4. Microscopic observation of Larmor precession dynamics in a spin-9/2 system. (a) Scheme of the precession sequence. 1. Preparation: we optically pump all atoms in $m_F = -9/2$ and take a reference image. 2. Precession: a sudden rotation of the magnetic field initiates Larmor precession dynamics. 3. Measurement: after a certain precession time, t_p , we quench back the field to its original orientation and perform the spin-resolved imaging protocol. (b) Sample snapshots of the reconstructed spin occupation at different precession times, t_p . The spin evolves from $-9/2$ to $+9/2$ over $T/2$ with $T = 40.16(6)$ ms, from which we determine $B_y = 135.0(2)$ mG. (c) Top: Normalized overlap of the image corresponding to each spin, \mathcal{O}_{m_F} . Bottom: Total normalized overlap, \mathcal{O}_{tot} . The solid line shows theoretical predictions accounting for all relevant infidelities, with the period T as the only fitting parameter. The shaded region indicates the effect of the uncertainties in the infidelities. (d) Comparison of the measured \mathcal{O}_{m_F} with theory (solid lines). Data for each m_F are offset by $9/2 - |m_F|$ for clarity.

trices of all spin states, projecting out multi-detection events, which yields the total occupation n^{tot} . We then compute the corresponding normalized overlap, \mathcal{O}_{tot} . This analysis effectively eliminates the effect of spin depolarization (see App. F), and isolates the last remaining source of infidelity: vacuum-induced losses. We independently measure the vacuum lifetime in the lattice to be $\tau_{\text{vac}} = 94(3)$ s, which translates into a loss of $\mathcal{L}_{\text{vac}} = 0.95(3)\%$ for each spin-readout cycle of 900 ms. As a result, atoms in states with larger m_F experience greater losses, since they remain in the lattice for longer before being imaged. This behavior is visible in the bottom panel of Fig. 4(c) as a reduction of \mathcal{O}_{tot} at precession times when higher- m_F states are populated. The theory prediction (solid line) contains no fitting parameters other than the oscillation period.

Figure 4(d) compares the measured precession dynamics of each spin state, $\mathcal{O}_{m_F}(t_p)$, to the theoretical predictions that include all identified limiting mechanisms. We again observe excellent agreement without additional fitting parameters, showcasing our solid understanding of all processes underlying the detection protocol. For clarity, these mechanisms are summarized in Tab. I. Overall, this benchmarking establishes our spin-resolved detection as an ideally suited tool for characterizing $SU(N)$ Fermi-Hubbard systems.

Process	Quantity	Value	Section
Imaging	Pinning, $(1 - \mathcal{F}_{\text{pin}})$	7.5(7)%	Sec. II
	Hopping, \mathcal{H}	1.0(3)%	Sec. II
	Losses, \mathcal{L}	6.5(7)%	Sec. II
	Spin depolarization	4.2(4)%	Sec. IV
	Vacuum losses, \mathcal{L}_{vac}	0.95(3)%	Sec. V
	Reconstruction	1.1(2)%	App. C
	Spin selectivity	<3.6(7)%	App. D
Optical pumping	Stretched pulse, $(1 - \mathcal{F}_{\text{OP},1})$	4.4(8)%	Sec. III
	Other pulses, $(1 - \mathcal{F}_{\text{OP},2})$	0.2(1)%	Sec. III
Spin removal	Inefficiency	<0.5(2)%	Sec. IV

TABLE I. Overview of the mechanisms limiting the imaging protocol and their corresponding infidelities. The last column indicates the section of the manuscript in where each process is identified and quantified.

VI. CONCLUSION

In this work, we demonstrate quantum-gas microscopy of ^{87}Sr in a Hubbard-regime optical lattice using a narrow-line imaging scheme. By combining spin-selective optical pumping with spin-resolved single-atom fluorescence imaging, we implement a protocol that sequentially images all 10 nuclear spin states of ^{87}Sr within a single experimental cycle. We benchmark the performance of our scheme by probing the coherent precession of an

$F = 9/2$ nuclear spin, finding excellent agreement with theoretical expectations. These results confirm that all processes underlying the detection protocol are well controlled and provide a clear route to further increase the pinning fidelity, which already exceeds 92%.

A natural next step is the microscopic characterization of $SU(N)$ degenerate Fermi gases of ^{87}Sr with a tunable number of components [47, 51], as well as the preparation and site-resolved study of $SU(N)$ fermionic Mott insulators. An additional possibility at the Mott temperature scale is to engineer artificial gauge fields by exploiting the nuclear spin states of the ground-state manifold as a synthetic dimension [53, 54, 80–82], which open the door to microscopic investigations of quantum-Hall physics in strongly correlated regimes.

At lower temperatures, $SU(N)$ systems are expected to host a wealth of unconventional quantum-magnetic phases. In particular, nearest-neighbor spin correlations, which so far have only been accessed via global probes [58], should be readily accessible. Below the super-exchange energy scale, a realistic target for future studies is the $SU(3)$ case, where a transition from diagonal stripe order to zigzag antiferromagnetism is expected upon decrease of the interaction strength [37, 42]. There, site-resolved detection should allow discriminating between competing theoretical scenarios in the intermediate-coupling regime [42–44]. Another promising direction is to study $SU(N)$ systems with tunable lattice geometries [83, 84], particularly in regimes where unconstrained magnetism and frustration govern the behavior of the system. For larger N , even more exotic magnetically ordered states have been predicted [37, 38, 40], and quantum-gas microscopy may provide decisive insight into whether the $SU(N)$ Hubbard model can stabilize a chiral spin liquid phase for $N > 5$ [36].

Beyond quantum simulation, the state-resolved detection technique developed here may have applications in other areas involving ^{87}Sr . In optical lattice clocks, ground-state population detection could enable novel erasure-conversion strategies [85] and improve coherence times. Combined with coherent control of the nuclear spin [32], our approach also provides a scalable platform for qudit-based quantum computing [23, 31].

Note added. During the writing of the manuscript we became aware of related experiments on free-space imaging of a single ^{87}Sr atom in an optical tweezer [86].

ACKNOWLEDGMENTS

We acknowledge insightful discussions with K. Hazard, M. Robert-de-Saint-Vincent, F. Schreck, D. Wilkowski, as well as with the members of the ICFO Quantum Gases Experimental group. We thank F. Faisant, S. Hirthe and Q. Redon for a careful reading of the manuscript. We acknowledge funding from the European Union (HORIZON-CL4-2022-QUANTUM-02-SGA through project PASQuanS2.1 No. 101113690

and ERC CoG project No. 101003295 SuperComp), the Spanish Ministry of Science and Innovation MCIU/AEI/10.13039/501100011033 (projects MAPS PID2023-149988NB-C22, and QuantERA DYNAMITE PCI2022-132919 with funding from European Union NextGenerationEU, PRTR-C17.I1 with funding from European Union NextGenerationEU and Generalitat de Catalunya, and Severo Ochoa CEX2024-001490-S), Fundació Cellex, Fundació Mir-Puig, and Generalitat de Catalunya (“Quàntica – Vall de la Mediterrània de les Ciències i les Tecnologies Quàntiques” Government Agreement GOV/51/2022 promoted by Secretariat of Digital Policies of the Government of Catalonia, and CERCA program). C.G. acknowledges support from MCIU/AEI/10.13039/501100011033/FEDER, EU and ESF+ (PREP2023-002109), A.R. from the “la Caixa” Foundation (ID 100010434) with fellowship code LCF/BQ/PI24/12050012, S.B. from MCIU/AEI/10.13039/501100011033 and ESF (PRE2020-094414), L.B. from Generalitat de Catalunya and ESF+ (FI-STEP 2025 STEP00008), and J.H. from the European Union (Marie Skłodowska-Curie-713729).

Appendix A: Details on the experimental setup

The preparation of the atomic cloud follows the standard laser cooling of ^{87}Sr [65]. The experiment begins with a continuously repumped magneto-optical trap (MOT) on the broad-linewidth transition at 461 nm ($^1S_0 \rightarrow ^1P_1$), as discussed in our previous works [61, 87]. This allows us to capture and precool the atoms down to mK temperatures. We then transfer the atoms to a narrow-line MOT on the red transition at 689 nm ($^1S_0 \rightarrow ^3P_1$), reaching temperatures on the order of 1 μK . During this process, we address two hyperfine states simultaneously. On the one hand, the transition to 3P_1 , $F' = 11/2$ is used to cool and trap the atoms. On the other hand, the 3P_1 , $F' = 9/2$ transition is used to mix the m_F spin states for efficient cooling in the MOT [65], which results in an equal distribution of the atoms in the ten Zeeman sublevels after the MOT.

In the next step, we load the laser-cooled atoms from the narrow-line MOT into a crossed optical dipole trap at 1064 nm, consisting of two perpendicular beams with a beam waist of approximately 100 μm and a trap depth of 16 μK . The optical dipole trap is then superimposed with a light sheet beam with 3.5 $\mu\text{m} \times 60 \mu\text{m}$ waist at 813.4 nm, which gives rise to a tight vertical confinement. After loading the cloud in these optical potentials, we adiabatically turn off the optical dipole trap while ramping the light sheet trap depth from 90 μK to 55 μK . Finally, we ramp up the optical lattice potential, generated by the four-fold interference of a single laser beam operating at 813.4 nm.

The final potential in which we image the fermionic strontium atoms consists of the light sheet beam at a depth of 55 μK and the optical lattice at a depth of

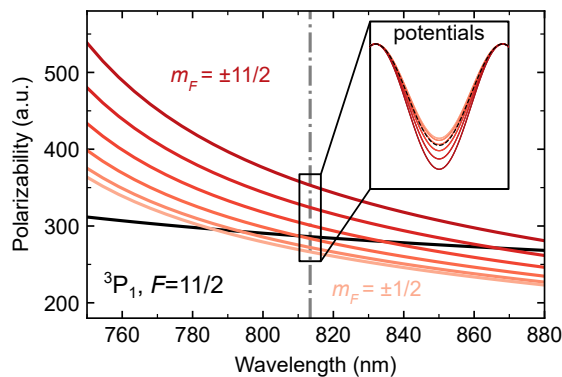


FIG. 5. Atomic polarizability for the 1S_0 (black line) and 3P_1 $F = 11/2$ states (red lines) as a function of wavelength for π -polarized trapping light. The gray dotted-dashed line indicates the trapping wavelength in our experiment, 813.4 nm. The inset shows schematically the potential of a certain lattice site for the different states. The polarizabilities are shown in atomic units (a.u.).

80 μK , corresponding to $460 E_r$, where $E_r = h^2/2m\lambda^2 \approx h \times 3.5 \text{ kHz}$ is the recoil energy of the lattice beam photons with m the mass of ^{87}Sr . Both are linearly polarized along the vertical direction, parallel to the direction of the bias magnetic field. This results in a vertical confinement of $\omega_z \approx 2\pi \times 6.6 \text{ kHz}$ and on-site trap frequencies $\omega_{x,\text{site}} \approx 2\pi \times 107 \text{ kHz}$ and $\omega_{y,\text{site}} \approx 2\pi \times 98 \text{ kHz}$. We also measure the lattice spacings from the fluorescence single-atom images to be $a_x \approx 606 \text{ nm}$ and $a_y \approx 549 \text{ nm}$. From this we conclude that the lattice beam crosses at an angle of 95.6° .

Appendix B: In-lattice cooling

As discussed in Sec. II, cooling is typically required to obtain enough signal from each strontium atom during fluorescence imaging. The specific cooling process depends on the difference between the polarizability of the ground state, α_g , with respect to the polarizability of the target excited state, α_e . When $\alpha_e \neq \alpha_g$ one can exploit the narrow line to excite the atom in specific regions of the trap and allow it to evolve on the differently confined excited-state potential. Then, on average, the atom decays back to the ground-state potential at a potential energy higher (lower) than the starting one, producing a net loss of kinetic energy per optical cycle. This process is known as attractive (repulsive) Sisyphus cooling for $\alpha_e > \alpha_g$ ($\alpha_e < \alpha_g$) and has been demonstrated in optical tweezer and lattice setups [61, 64, 66, 68, 70]. Instead, when $\alpha_g = \alpha_e$ one may spectroscopically resolve the sideband between the different motional eigenstates which allows to perform resolved sideband cooling [66, 67].

Figure 5 shows the polarizabilities for the ground and excited 3P_1 $F' = 11/2$ states of ^{87}Sr . The optical potential at 813.4 nm traps both manifolds, as indicated by the positive sign of the polarizabilities. However, in

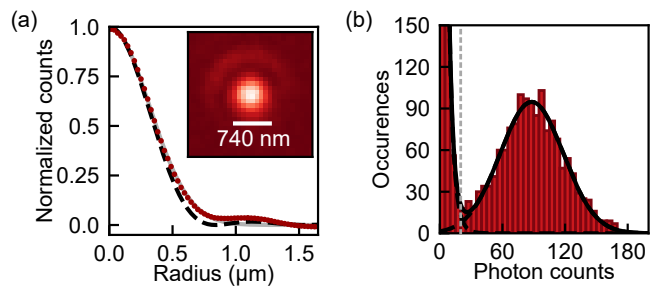


FIG. 6. Imaging resolution and occupation reconstruction. (a) Azimuthal average of the measured point spread function (PSF) of our imaging system, compared to a Gaussian fit (gray line) and diffraction-limited Airy disk (black dashed line). The inset shows the PSF obtained by averaging over 199 isolated atoms. (b) Histogram of the photon counts per lattice site accumulated over 64 images with an average filling of about 2% in a region of 31×31 sites. We clearly see a separation between the background noise peak around zero counts and the atom signal peak centered at about 95 photon counts.

our configuration there is a tensor contribution on the 3P_1 manifold. This results in states with higher $|m_F|$ having a larger polarizability than the ground states, while those with lower $|m_F|$ have a lower polarizability. As we perform imaging and cooling on the cycling $^1S_0 |9/2, -9/2\rangle \rightarrow ^3P_1 |11/2, -11/2\rangle$ transition, where $\alpha_g/\alpha_e \approx 0.8$, we satisfy the conditions for efficient attractive Sisyphus cooling.

By tuning the frequency of the light, efficient heating is also possible. We exploit this to achieve a selective spin removal used in the imaging protocol presented in Sec. IV. This pulse consists of a 6 ms exposure with blue-detuned light, sweeping the frequency from 7 to 90 Γ from the imaging transition. This results in heating of the atoms populating the stretched state, that eventually escape the optical trapping potential.

Appendix C: Imaging reconstruction

In order to extract the atomic occupations $n_{i,j}$ from each snapshot, we follow a procedure of image deconvolution. Specifically, we run 50 iterations of the Richardson-Lucy deconvolution [61, 88] based on the measured point spread function of our imaging setup, shown in Fig. 6(a). This allows us to extract a histogram of the photon counts in each lattice site for a set of images with a sparse filling of 2% over 31×31 lattice sites, see Fig. 6(b). We clearly distinguish empty and filled sites with a threshold of 20 photons (gray dashed line). We quantify the distinguishability by computing the overlap in between fitted noise and signal distributions. More specifically, we define the reconstruction infidelity as the area of the signal distribution below threshold, 1.1(2)%. Its counterpart, the false positive probability, is defined as the area of the noise distribution above threshold, 0.51(5)%.

When reconstructing pictures with high atomic density, such as the right snapshot of Fig. 1(d), the performance of our method is reduced. In order to count the atoms in such high-density images, we follow the reconstruction procedure described in [89].

Appendix D: Narrow-line optical pumping

1. Details on the optical pumping pulses

The narrow-line optical pumping in our experiment addresses the $^1S_0, F = 9/2 \rightarrow ^3P_1, F' = 9/2$ hyperfine manifolds. The choice of this particular line comes from the similarity of the Clebsch-Gordan coefficients for all transitions, in contrast to the very asymmetric values in the $^1S_0, F = 9/2 \rightarrow ^3P_1, F' = 11/2$. Additionally, this manifold displays a convenient Zeeman splitting that allows us to resolve all transitions at the imaging B-field of approximately 20 G within the bandwidth of a double-pass acousto-optic modulator. All optical pumping pulses used in this work were performed with an intensity of approximately $15 I_{\text{sat}}$ and a pulse duration of 2 ms. To improve pumping fidelities, we always pumped the atoms with two consecutive sets of pulses.

From the results in Sec. III, we identified a significant difference between the optical pumping fidelities $\mathcal{F}_{\text{OP},1}$ (pulse from $m_F = -7/2$ to the $m_F = -9/2$ state) and $\mathcal{F}_{\text{OP},2}$ (optical pumping in the central states). This observation can be explained by experimental imperfections that affect the two processes in a different way. In the first case, a finite fraction η of π -polarized light in the optical pumping beam will lead to a residual steady-state population η in the $m_F = -7/2$ state due to the two competing optical pumping processes between $m_F = -7/2$ and $m_F = -9/2$. In contrast, during optical pumping of the intermediate states, the same defect has negligible impact as additional spin states become populated, eventually depleting the state of origin.

2. Spin selectivity

We use the measurement scheme presented in Fig. 2(a) to provide a bound on the spin selectivity of the imaging. Specifically, we use the residual signal in the image taken after the depumping step to bound the fraction of the population in other spins which is affected by the imaging light. This corresponds to 0.5(1) atoms on average out of the 25(2) atoms detected in the reference image. After the depumping pulse, the atoms are approximately distributed among $m_F = -7/2$ and $-5/2$ in a 60/40 ratio, respectively, according to the corresponding Clebsch-Gordan coefficients. This way, any atom detected in the subsequent image was either not depumped from the stretched state or was transferred off-resonantly to $m_F = -9/2$ from the other states by the imaging light. Since off-resonant scattering decays

quadratically with detuning, it is reasonable to assume that most atoms that undergo this process come from the $m_F = -7/2$ state. From these observations, we conclude that $< 3.6(7)\%$ of the atoms in the $m_F = -7/2$ state are detected during imaging.

3. Optical pumping spectrum

To characterize the iterative optical pumping schemes used in the main text, we directly measure the spectrum of the involved optical pumping transitions. We follow a similar procedure to that of Sec. III, but in this case scanning the detuning of one of the optical pumping pulses (see Fig. 7(a)). First, we prepare all atoms in the $m_F = -9/2$ spin state and take a reference image. Then, we pump them to states m_F and $m_F + 1$. Finally, we bring them back to the original state and take a second image. In the retrieval stage, the frequency of the first pulse, i.e., the one addressing the $m_F + 1$ state, is modified in each experimental sequence, which allows us to locate the specific resonance. From the two measured images, we can extract the normalized overlap \mathcal{O} , which we plot as a function of the detuning δ_{pump} in Fig. 7(b). Repeating the process scanning the different retrieval pulses we obtain the 9 plotted resonances, each colored consistently with the specific retrieved $m_F + 1$ state. We apply Gaussian fits to extract the resonant frequencies and plot them in the energy diagram in Fig. 7(c). Here, we clearly see how the relative spacing of subsequent resonances increases as we address higher m_F states, ranging from 1–2 MHz approximately. We fit the data with the energy curve stemming from the joint contribution of Zeeman and AC Stark shifts, and using the magnetic field as the only free parameter. This yields the red dashed curve, which shows optimal agreement, slightly correcting the magnetic field to $B = 19.2$ G.

Each of the measured resonances shows a baseline value of \mathcal{O} . This finite value can be understood by considering the atoms that populate the m_F state after the depumping stage, as these atoms are successfully retrieved independently of the pulse addressing the $m_F + 1$ state. Following a similar approach, we also measure the resonance $^1S_0 |9/2, +7/2\rangle \rightarrow ^3P_1 |9/2, +9/2\rangle$, which is not shown in Fig. 7(b), since it can be only addressed through a σ^+ pulse. In this case, we optically pump the atoms all the way down to the $m_F = +9/2$ state, scanning the frequency of the last depumping pulse, $^3P_1 |9/2, +9/2\rangle$. Next, we retrieve and image only the atoms in the $m_F = +7/2$ state. In that case, the resonance is obtained by finding a minimum instead of a maximum in the normalized overlap. The extracted resonance is also shown in Fig. 7(b).

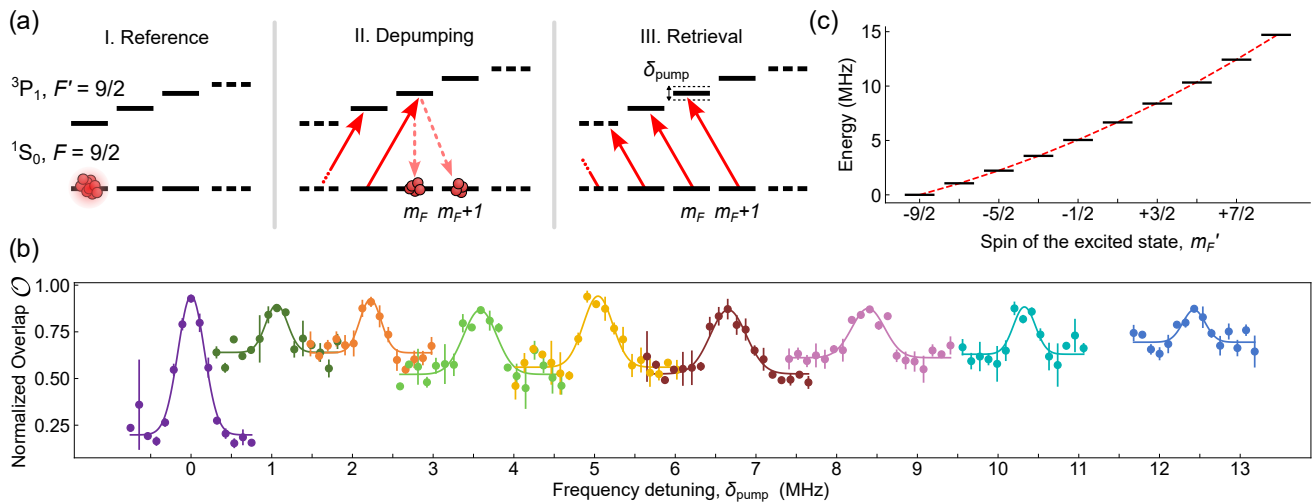


FIG. 7. Hyperfine spectrum of the $^3P_1, F' = 9/2$ optical pumping transition. (a) We initialize the system in the $-9/2$ spin state and image its occupation in the lattice (left panel). We then populate the pair of spin states m_F and $m_F + 1$ through optical pumping (central panel). Finally, we apply the retrieval pulses to bring the atomic population back to the imaging state and detect the atomic cloud again (right panel). In this last step, the frequency of the pulse that addresses the $m_F + 1$ state is scanned with δ_{pump} to measure the corresponding resonance. (b) Measurement of the hyperfine spectrum using the method described in (a). The color coding matches the one used in the main text for the different m_F states, considering here the ground m_F state addressed by each transition. The resonances appear well resolved, with a splitting that increases for higher m_F values. (c) Energy splitting of the excited state manifold. The energies correspond to the peaks of the resonances measured in (b), extracted with a Gaussian fit. The dashed red line fits the data to the theoretical Zeeman and AC Stark shifts, using only the magnetic field as a free parameter.

Appendix E: Spin population and off-resonant Raman scattering

In Sec. IV we presented the ability of our experiment to detect the populations of the 10 different spin states of ^{87}Sr . In Fig. 8(a), we show the averaged spin populations measured in SU(10) thermal clouds. Specifically, we plot the ratio of the number of atoms detected in image α , N_α to the total number of atoms N . We find that on average (40 repetitions) the atoms are equally distributed between the 10 spin states. A single repetition of this data set is displayed in the diagonal axis of Fig. 3(c). In that same measurement, we observed 7 multi-detection events appearing in the first ($d = 1$) off-diagonal of the image-to-image detection coincidences. In Fig. 8(b) we study the contributions in more detail by plotting the sum of the overlap for the d^{th} off-diagonal axis, $N_{\text{off}} = \sum_\alpha N_{\alpha, \alpha+d}$, where α is the image number. We find that the main contribution arises for the first off-diagonal, $d = 1$, with 2.8(4)%, corresponding to atoms detected in subsequent images. This nearest-snapshot off-diagonal contribution is consistent with induced depolarization during the 300 ms imaging exposure.

The origin of such process is, mainly, the 813.4 nm light generating the optical potential which causes off-resonant Raman scattering from the excited $^3P_1 |11/2, -11/2\rangle$ over the 3P_J manifold via higher excited states. Following Ref. [77], we estimate the total rate into other 3P_1 states to be on the order of 1 s^{-1} . As, upon decay-

ing to the ground manifold, these atoms may end up in states with $m_F \neq -9/2$, this directly leads to spin depolarization. Furthermore, we estimate that the total rate into the metastable $^3P_{0,2}$ manifolds is also on the order of 1 s^{-1} . This results in a population build-up in these metastable states due to their long lifetime. The use of repumpers during imaging, in our case 679 nm for the 3P_0 and 707 nm for the 3P_2 , solves this issue, returning the entire population to the ground state manifold. However, this effect still contributes to spin depolarization. In particular, the difference between the initial $m_F = -9/2$ and the final one depends on how many repumping cycles are needed to get the atom back to the ground state, which makes it more likely for the atoms to end up in close-by m_F states, as observed. Overall, we measure the depolarization during an imaging cycle to be 4.2(4)%, which is consistent with the estimated rates provided.

Appendix F: Spin-9/2 precession

In Sec. V, we benchmark our spin-resolved imaging protocol through the observation of a spin-9/2 Larmor precession. Here, we describe this effect involving only the ground-state manifold.

Let us consider an atom with spin $m_F = -9/2$ along the quantization axis \hat{e}_z , and introduce a sudden rotation in the magnetic field, defining it along \hat{e}_y with a field B_p . The initial state upon this quench can now be expressed

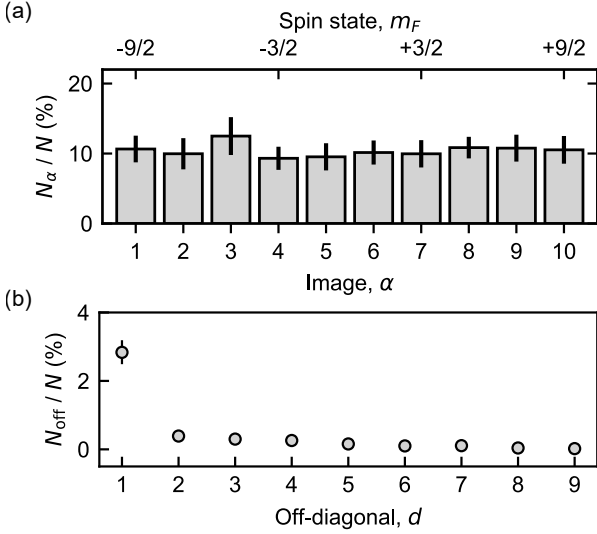


FIG. 8. Spin population distribution in SU(10) systems. (a) The atom number N_α detected in each spin state is normalized by the total atom number N and averaged over 40 repetitions. The errorbars denote the standard deviation. (b) Plot of the number of off-diagonal events $N_{\text{off}} = \sum_\alpha N_{\alpha, \alpha+d}$ for the different off-diagonals, d . The main contribution arises from the first off-diagonal $d = 1$, where we find 2.8(4)%. The error bars represent a confidence interval of 95% obtained from 1000 bootstrap samples.

in terms of the new basis,

$$|9/2, -9/2\rangle_z = \sum_k c_k |9/2, m_k\rangle_y, \quad (\text{F1})$$

where c_k are the complex coefficients and $|9/2, m_k\rangle_y$ are the 10 Zeeman states defined along the y direction. The unitary dynamics under this new configuration can be expressed as

$$|\Psi(t)\rangle = \sum_k c_k e^{-iE_k t/\hbar} |9/2, m_k\rangle_y, \quad (\text{F2})$$

where E_k is the energy of each spin state $E_k = g_F \mu_0 B_p m_k$. This evolution leads to precession dynamics, with periodic magnetization revivals with a period $T = \hbar/(g_F \mu_0 B_p)$. Upon quenching back the quantization axis along \hat{e}_z , the state is projected back onto the original basis. In this way, the measured populations in a certain m_F will be given by ${}_z\langle 9/2, m_F | \Psi(t) \rangle^2$.

In order to compare numerics with our experimental results, we need to take into account the fidelity of the different processes taking place during the imaging protocol. Specifically, we consider the pinning fidelity to express the normalized overlap for $m_F = -9/2$ as $\mathcal{O}_{-9/2} = \mathcal{F}_{\text{pin}} {}_z\langle 9/2, -9/2 | \Psi(t) \rangle^2$. For all other states, we additionally account for the corresponding optical pumping fidelity and vacuum losses. We write

$$\mathcal{O}_{m_F} = f_{m_F} {}_z\langle 9/2, m_F | \Psi(t) \rangle^2,$$

where

$$f_{m_F} = \mathcal{F}_{\text{pin}} \mathcal{F}_{\text{OP},1} (\mathcal{F}_{\text{OP},2})^{7/2+m_F} (1 - \mathcal{L}_{\text{vac}})^{9/2+m_F}$$

is the resulting correction factor. Specifically, we consider the vacuum losses over the number of imaging cycles prior to the image for each m_F , comprising 300 ms exposure and 600 ms for camera readout, spin removal and optical pumping. For the last spin state, $m_F = +9/2$, they accumulate to $(1 - \mathcal{L}_{\text{vac}})^9 = 9.2(3)\%$.

The total occupation matrix n^{tot} , introduced in Sec. V, is mostly agnostic to spin effects. The reason for this is that an atom that is not detected in the image for its corresponding spin due to failed optical pumping or spin depolarization is likely to be imaged in a subsequent image. This is true for all images except the last. As the pinning fidelity is mainly limited by spin depolarization, we can ignore its contribution when estimating \mathcal{O}_{tot} , and instead consider the hopping rate \mathcal{H} and the vacuum losses during the imaging procedure. In a similar manner, it seems that the pumping fidelities $\mathcal{F}_{\text{OP},1}$ and $\mathcal{F}_{\text{OP},2}$ mostly reflect populations that do not reach the target spin state after optical pumping, but not atoms abandoning their respective lattice sites. For this reason, we neglect the optical pumping fidelities as well and we estimate the total overlap as

$$\mathcal{O}_{\text{tot}} = \sum_{m_F=-9/2}^{7/2} f'_{m_F} {}_z\langle 9/2, m_F | \Psi(t) \rangle^2 + f_{9/2} {}_z\langle 9/2, 9/2 | \Psi(t) \rangle^2,$$

with a factor

$$f'_{m_F} = (1 - \mathcal{H} - \mathcal{L}_{\text{vac}})(1 - \mathcal{L}_{\text{vac}})^{9/2+m_F}.$$

These estimations allow us to calculate the dynamics of the measured states that are compared with the experimental results in the main text.

-
- [1] A. Browaeys and T. Lahaye, Many-body physics with individually controlled Rydberg atoms, *Nat. Phys.* **16**, 132 (2020).
- [2] C. Gross and W. S. Bakr, Quantum gas microscopy for single atom and spin detection, *Nat. Phys.* **17**, 1316 (2021).
- [3] M. F. Parsons, A. Mazurenko, C. S. Chiu, G. Ji, D. Greif, and M. Greiner, Site-resolved measurement of the spin-correlation function in the Fermi-Hubbard model, *Science* **353**, 1253 (2016).
- [4] L. W. Cheuk, M. A. Nichols, K. R. Lawrence, M. Okan, H. Zhang, E. Khatami, N. Trivedi, T. Paiva, M. Rigol, and M. W. Zwierlein, Observation of spatial charge and spin correlations in the 2D Fermi-Hubbard model, *Science* **353**, 1260 (2016).
- [5] M. Boll, T. A. Hilker, G. Salomon, A. Omran, J. Nespolo, L. Pollet, I. Bloch, and C. Gross, Spin- and density-resolved microscopy of antiferromagnetic correlations in Fermi-Hubbard chains, *Science* **353**, 1257 (2016).
- [6] T. Fukuhara, A. Kantian, M. Endres, M. Cheneau, P. Schauß, S. Hild, D. Bellem, U. Schollwöck, T. Gimarchi, C. Gross, I. Bloch, and S. Kuhr, Quantum dynamics of a mobile spin impurity, *Nat. Phys.* **9**, 235 (2013).
- [7] D. Wei, A. Rubio-Abadal, B. Ye, F. Machado, J. Kemp, K. Srakaew, S. Hollerith, J. Rui, S. Gopalakrishnan, N. Y. Yao, I. Bloch, and J. Zeiher, Quantum gas microscopy of Kardar-Parisi-Zhang superdiffusion, *Science* **376**, 716 (2022).
- [8] H. Labuhn, D. Barredo, S. Ravets, S. de Léséleuc, T. Macrì, T. Lahaye, and A. Browaeys, Tunable two-dimensional arrays of single Rydberg atoms for realizing quantum Ising models, *Nature* **534**, 667–670 (2016).
- [9] H. Bernien, S. Schwartz, A. Keesling, H. Levine, A. Omran, H. Pichler, S. Choi, A. S. Zibrov, M. Endres, M. Greiner, V. Vuletić, and M. D. Lukin, Probing many-body dynamics on a 51-atom quantum simulator, *Nature* **551**, 579–584 (2017).
- [10] S. de Léséleuc, V. Lienhard, P. Scholl, D. Barredo, S. Weber, N. Lang, H. P. Büchler, T. Lahaye, and A. Browaeys, Observation of a symmetry-protected topological phase of interacting bosons with Rydberg atoms, *Science* **365**, 775 (2019).
- [11] J. Koepsell, S. Hirthe, D. Bourgund, P. Sompet, J. Vijayan, G. Salomon, C. Gross, and I. Bloch, Robust bilayer charge pumping for spin- and density-resolved quantum gas microscopy, *Phys. Rev. Lett.* **125**, 010403 (2020).
- [12] Z. Z. Yan, B. M. Spar, M. L. Prichard, S. Chi, H.-T. Wei, E. Ibarra-García-Padilla, K. R. A. Hazzard, and W. S. Bakr, Two-dimensional programmable tweezer arrays of fermions, *Phys. Rev. Lett.* **129**, 123201 (2022).
- [13] T.-Y. Wu, A. Kumar, F. Giraldo, and D. S. Weiss, Stern–Gerlach detection of neutral-atom qubits in a state-dependent optical lattice, *Nat. Phys.* **15**, 538 (2019).
- [14] D. Bluvstein, A. A. Geim, S. H. Li, S. J. Evered, J. P. B. Ataiades, G. Baranes, A. Gu, T. Manovitz, M. Xu, M. Kalinowski, S. Majidy, C. Kokail, N. Maskara, E. C. Trapp, L. M. Stewart, S. Hollerith, H. Zhou, M. J. Gullans, S. F. Yelin, M. Greiner, V. Vuletić, M. Cain, and M. D. Lukin, A fault-tolerant neutral-atom architecture for universal quantum computation, *Nature* **649**, 39 (2026).
- [15] A. Widera, F. Gerbier, S. Fölling, T. Gericke, O. Mandel, and I. Bloch, Coherent collisional spin dynamics in optical lattices, *Phys. Rev. Lett.* **95**, 190405 (2005).
- [16] J. S. Krauser, J. Heinze, N. Fläschner, S. Götze, C. Becker, and K. Sengstock, Coherent multi-flavour spin dynamics in a fermionic quantum gas, *Nat. Phys.* **8**, 813 (2012).
- [17] A. de Paz, A. Chotia, E. Maréchal, P. Pedri, L. Vernac, O. Gorceix, and B. Laburthe-Tolra, Resonant demagnetization of a dipolar bose-einstein condensate in a three-dimensional optical lattice, *Phys. Rev. A* **87**, 051609 (2013).
- [18] A. Patscheider, B. Zhu, L. Chomaz, D. Petter, S. Baier, A.-M. Rey, F. Ferlaino, and M. J. Mark, Controlling dipolar exchange interactions in a dense three-dimensional array of large-spin fermions, *Phys. Rev. Res.* **2**, 023050 (2020).
- [19] T. B. Ottenstein, T. Lompe, M. Kohnen, A. N. Wenz, and S. Jochim, Collisional stability of a three-component degenerate Fermi gas, *Phys. Rev. Lett.* **101**, 203202 (2008).
- [20] J. H. Huckans, J. R. Williams, E. L. Hazlett, R. W. Stites, and K. M. O’Hara, Three-body recombination in a three-state fermi gas with widely tunable interactions, *Phys. Rev. Lett.* **102**, 165302 (2009).
- [21] J. Mongkolkiattichai, L. Liu, S. Dasgupta, K. R. A. Hazzard, and P. Schauss, Quantum gas microscopy of three-flavor Hubbard systems, arXiv:2503.05687 (2025).
- [22] T. Bothwell, C. J. Kennedy, A. Aeppli, D. Kedar, J. M. Robinson, E. Oelker, A. Staron, and J. Ye, Resolving the gravitational redshift across a millimetre-scale atomic sample, *Nature* **602**, 420 (2022).
- [23] A. J. Daley, M. M. Boyd, J. Ye, and P. Zoller, Quantum Computing with Alkaline-Earth-Metal Atoms, *Phys. Rev. Lett.* **101**, 170504 (2008).
- [24] K. Barnes, P. Battaglino, B. J. Bloom, K. Cassella, R. Coxe, N. Crisosto, J. P. King, S. S. Kondov, K. Kotru, S. C. Larsen, J. Lauigan, B. J. Lester, M. McDonald, E. Megidish, S. Narayanaswami, C. Nishiguchi, R. Notermans, L. S. Peng, A. Ryou, T.-Y. Wu, and M. Yarwood, Assembly and coherent control of a register of nuclear spin qubits, *Nature Communications* **13**, 2779 (2022).
- [25] W. Huie, L. Li, N. Chen, X. Hu, Z. Jia, W. K. C. Sun, and J. P. Covey, Repetitive readout and real-time control of nuclear spin qubits in ^{171}Yb atoms, *PRX Quantum* **4**, 030337 (2023).
- [26] A. Jenkins, J. W. Lis, A. Senoo, W. F. McGrew, and A. M. Kaufman, Ytterbium nuclear-spin qubits in an optical tweezer array, *Phys. Rev. X* **12**, 021027 (2022).
- [27] S. Ma, A. P. Burgers, G. Liu, J. Wilson, B. Zhang, and J. D. Thompson, Universal gate operations on nuclear spin qubits in an optical tweezer array of ^{171}Yb atoms, *Phys. Rev. X* **12**, 021028 (2022).
- [28] M. A. Norcia, W. B. Cairncross, K. Barnes, P. Battaglino, A. Brown, M. O. Brown, K. Cassella, C.-A. Chen, R. Coxe, D. Crow, J. Epstein, C. Griger, A. M. W. Jones, H. Kim, J. M. Kindem, J. King, S. S. Kondov, K. Kotru, J. Lauigan, M. Li, M. Lu, E. Megidish, J. Marjanovic, M. McDonald, T. Mittiga,

- J. A. Muniz, S. Narayanaswami, C. Nishiguchi, R. Noter-
mans, T. Paule, K. A. Pawlak, L. S. Peng, A. Ryou,
A. Smull, D. Stack, M. Stone, A. Sucich, M. Urbanek,
R. J. M. van de Veerdonk, Z. Vendeiro, T. Wilkason,
T.-Y. Wu, X. Xie, X. Zhang, and B. J. Bloom, Midcir-
cuit qubit measurement and rearrangement in a ^{171}Yb
atomic array, *Phys. Rev. X* **13**, 041034 (2023).
- [29] D. González-Cuadra, D. Bluvstein, M. Kalinowski,
R. Kaubruegger, N. Maskara, P. Naldesi, T. V. Zache,
A. M. Kaufman, M. D. Lukin, H. Pichler, B. Vermersch,
J. Ye, and P. Zoller, Fermionic quantum processing with
programmable neutral atom arrays, *Proceedings of the
National Academy of Sciences* **120**, e2304294120 (2023).
- [30] T. V. Zache, D. González-Cuadra, and P. Zoller,
Fermion-qudit quantum processors for simulating lattice
gauge theories with matter, *Quantum* **7**, 1140 (2023).
- [31] S. Omanakuttan, A. Mitra, M. J. Martin, and I. H.
Deutsch, Quantum optimal control of ten-level nuclear
spin qudits in ^{87}Sr , *Phys. Rev. A* **104**, L060401 (2021).
- [32] H. Ahmed, A. Litvinov, P. Guesdon, E. Maréchal,
J. Huckans, B. Pasquiou, B. Laburthe-Tolra, and
M. Robert-de Saint-Vincent, Coherent control over the
high-dimensional space of the nuclear spin of alkaline-
earth atoms, *PRX Quantum* **6**, 020352 (2025).
- [33] M. A. Cazalilla and A. M. Rey, Ultracold Fermi gases
with emergent $SU(N)$ symmetry, *Rep. Prog. Phys.* **77**,
124401 (2014).
- [34] E. Ibarra-García-Padilla and S. Choudhury, Many-body
physics of ultracold alkaline-earth atoms with $SU(N)$ -
symmetric interactions, *Journal of Physics: Condensed
Matter* **37**, 083003 (2024).
- [35] S. Stellmer, R. Grimm, and F. Schreck, Detection and
manipulation of nuclear spin states in fermionic stron-
tium, *Phys. Rev. A* **84**, 043611 (2011).
- [36] M. Hermele, V. Gurarie, and A. M. Rey, Mott Insulators
of Ultracold Fermionic Alkaline Earth Atoms: Undercon-
strained Magnetism and Chiral Spin Liquid, *Phys. Rev.
Lett.* **103**, 135301 (2009).
- [37] T. A. Tóth, A. M. Läuchli, F. Mila, and K. Penc, Three-
sublattice ordering of the $SU(3)$ Heisenberg model of
three-flavor fermions on the square and cubic lattices,
Phys. Rev. Lett. **105**, 265301 (2010).
- [38] P. Corboz, A. M. Läuchli, K. Penc, M. Troyer, and
F. Mila, Simultaneous Dimerization and $SU(4)$ Symme-
try Breaking of 4-Color Fermions on the Square Lattice,
Phys. Rev. Lett. **107**, 215301 (2011).
- [39] P. Nataf and F. Mila, Exact diagonalization of Heisenberg
 $SU(N)$ models, *Phys. Rev. Lett.* **113**, 127204 (2014).
- [40] P. Nataf, M. Lajkó, P. Corboz, A. M. Läuchli, K. Penc,
and F. Mila, Plaquette order in the $SU(6)$ Heisenberg
model on the honeycomb lattice, *Phys. Rev. B* **93**, 201113
(2016).
- [41] C. Romen and A. M. Läuchli, Structure of spin corre-
lations in high-temperature $SU(N)$ quantum magnets,
Phys. Rev. Res. **2**, 043009 (2020).
- [42] C. Feng, E. Ibarra-García-Padilla, K. R. A. Hazzard,
R. Scalettar, S. Zhang, and E. Vitali, Metal-insulator
transition and quantum magnetism in the $SU(3)$ Fermi-
Hubbard model, *Phys. Rev. Res.* **5**, 043267 (2023).
- [43] S. Bird, S. Huber, and J. Nys, Partial suppression of mag-
netism in the square lattice $SU(3)$ Hubbard model, *Phys.
Rev. B* **112**, L161115 (2025).
- [44] S. V. Klejweg and P. Corboz, Zigzag antiferromag-
nets in the $SU(3)$ Hubbard model on the square lattice,
arXiv:2506.14703 (2025).
- [45] H. Schlömer, F. Grusdt, U. Schollwöck, K. R. A. Haz-
zard, and A. Bohrdt, Subdimensional magnetic polarons
in the one-hole doped $SU(3)$ t - J model, *Phys. Rev. B*
110, 125134 (2024).
- [46] T. Fukuhara, Y. Takasu, M. Kumakura, and Y. Taka-
hashi, Degenerate Fermi gases of ytterbium, *Phys. Rev.
Lett.* **98**, 030401 (2007).
- [47] B. J. DeSalvo, M. Yan, P. G. Mickelson, Y. N. Mar-
tinez de Escobar, and T. C. Killian, Degenerate Fermi
gas of ^{87}Sr , *Phys. Rev. Lett.* **105**, 030402 (2010).
- [48] X. Zhang, M. Bishof, S. L. Bromley, C. V. Kraus, M. S.
Safronova, P. Zoller, A. M. Rey, and J. Ye, Spectroscopic
observation of $SU(N)$ -symmetric interactions in Sr or-
bital magnetism, *Science* **345**, 1467 (2014).
- [49] G. Pagano, M. Mancini, G. Cappellini, P. Lombardi,
F. Schäfer, H. Hu, X.-J. Liu, J. Catani, C. Sias, M. Ingus-
cio, and L. Fallani, A one-dimensional liquid of fermions
with tunable spin, *Nat. Phys.* **10**, 198 (2014).
- [50] B. Song, Y. Yan, C. He, Z. Ren, Q. Zhou, and G.-B. Jo,
Evidence for bosonization in a three-dimensional gas of
 $SU(N)$ fermions, *Phys. Rev. X* **10**, 041053 (2020).
- [51] L. Sonderhouse, C. Sanner, R. B. Hutson, A. Goban,
T. Bilitewski, L. Yan, W. R. Milner, A. M. Rey, and
J. Ye, Thermodynamics of a deeply degenerate $SU(N)$ -
symmetric Fermi gas, *Nat. Phys.* **16**, 1216 (2020).
- [52] S. Taie, R. Yamazaki, S. Sugawa, and Y. Takahashi, An
 $SU(6)$ Mott insulator of an atomic Fermi gas realized
by large-spin Pomeranchuk cooling, *Nat. Phys.* **8**, 825
(2012).
- [53] M. Mancini, G. Pagano, G. Cappellini, L. Livi, M. Rider,
J. Catani, C. Sias, P. Zoller, M. Inguscio, M. Dalmonte,
and L. Fallani, Observation of chiral edge states with
neutral fermions in synthetic Hall ribbons, *Science* **349**,
1510 (2015).
- [54] J. H. Han, J. H. Kang, and Y. Shin, Band Gap Closing in
a Synthetic Hall Tube of Neutral Fermions, *Phys. Rev.
Lett.* **122**, 065303 (2019).
- [55] C. Hofrichter, L. Riegger, F. Scazza, M. Höfer, D. R.
Fernandes, I. Bloch, and S. Fölling, Direct probing of
the Mott crossover in the $SU(N)$ Fermi-Hubbard model,
Phys. Rev. X **6**, 021030 (2016).
- [56] G. Pasqualetti, O. Bettermann, N. Darkwah Oppong,
E. Ibarra-García-Padilla, S. Dasgupta, R. T. Scalettar,
K. R. A. Hazzard, I. Bloch, and S. Fölling, Equation
of State and Thermometry of the 2D $SU(N)$ Fermi-
Hubbard Model, *Phys. Rev. Lett.* **132**, 083401 (2024).
- [57] D. Tusi, L. Franchi, L. F. Livi, K. Baumann, D. B.
Orenes, L. D. Re, R. E. Barfknecht, T.-W. Zhou, M. In-
guscio, G. Cappellini, M. Capone, J. Catani, and L. Fal-
lani, Flavour-selective localization in interacting lattice
fermions, *Nat. Phys.* **18**, 1201 (2022).
- [58] S. Taie, E. Ibarra-García-Padilla, N. Nishizawa,
Y. Takasu, Y. Kuno, H.-T. Wei, R. T. Scalettar, K. R. A.
Hazzard, and Y. Takahashi, Observation of antiferromag-
netic correlations in an ultracold $SU(N)$ Hubbard model,
Nat. Phys. **18**, 1356 (2022).
- [59] M. Miranda, R. Inoue, Y. Okuyama, A. Nakamoto, and
M. Kozuma, Site-resolved imaging of ytterbium atoms
in a two-dimensional optical lattice, *Phys. Rev. A* **91**,
063414 (2015).
- [60] R. Yamamoto, J. Kobayashi, T. Kuno, K. Kato, and
Y. Takahashi, An ytterbium quantum gas microscope
with narrow-line laser cooling, *New J. Phys.* **18**, 023016

- (2016).
- [61] S. Buob, J. Höschele, V. Makhalov, A. Rubio-Abadal, and L. Tarruell, A Strontium Quantum-Gas Microscope, *PRX Quantum* **5**, 020316 (2024).
- [62] C. S. Chiu, G. Ji, A. Mazurenko, D. Greif, and M. Greiner, Quantum state engineering of a Hubbard system with ultracold fermions, *Phys. Rev. Lett.* **120**, 243201 (2018).
- [63] A. Mazurenko, C. S. Chiu, G. Ji, M. F. Parsons, M. Kanász-Nagy, R. Schmidt, F. Grusdt, E. Demler, D. Greif, and M. Greiner, A cold-atom Fermi-Hubbard antiferromagnet, *Nature* **545**, 462 (2017).
- [64] A. Urech, I. H. A. Knottnerus, R. J. C. Spreeuw, and F. Schreck, Narrow-line imaging of single strontium atoms in shallow optical tweezers, *Phys. Rev. Res.* **4**, 023245 (2022).
- [65] T. Mukaiyama, H. Katori, T. Ido, Y. Li, and M. Kuwata-Gonokami, Recoil-limited laser cooling of ^{87}Sr atoms near the Fermi temperature, *Phys. Rev. Lett.* **90**, 113002 (2003).
- [66] A. Cooper, J. P. Covey, I. S. Madjarov, S. G. Porsev, M. S. Safronova, and M. Endres, Alkaline-Earth Atoms in Optical Tweezers, *Phys. Rev. X* **8**, 041055 (2018).
- [67] M. A. Norcia, A. W. Young, and A. M. Kaufman, Microscopic Control and Detection of Ultracold Strontium in Optical-Tweezer Arrays, *Phys. Rev. X* **8**, 041054 (2018).
- [68] R. Tao, M. Ammenwerth, F. Gyger, I. Bloch, and J. Zeiher, High-fidelity detection of large-scale atom arrays in an optical lattice, *Phys. Rev. Lett.* **133**, 013401 (2024).
- [69] R. Tao, O. Lib, F. Gyger, H. Timme, M. Ammenwerth, I. Bloch, and J. Zeiher, Universal gates for a metastable qubit in strontium-88, arXiv:2506.10714 (2025).
- [70] J. P. Covey, I. S. Madjarov, A. Cooper, and M. Endres, 2000-Times Repeated Imaging of Strontium Atoms in Clock-Magic Tweezer Arrays, *Phys. Rev. Lett.* **122**, 173201 (2019).
- [71] T. Chalopin, P. Bojović, S. Wang, T. Franz, A. Sinha, Z. Wang, D. Bourgund, J. Obermeyer, F. Grusdt, A. Bohrdt, L. Pollet, A. Wietek, A. Georges, T. Hilker, and I. Bloch, Observation of emergent scaling of spin-charge correlations at the onset of the pseudogap, *Proceedings of the National Academy of Sciences* **123**, e2525539123 (2026).
- [72] T. Hartke, B. Oreg, C. Feng, C. Turnbaugh, J. Hertkorn, Y.-Y. He, N. Jia, E. Khatami, S. Zhang, and M. Zwierlein, Competition of fermion pairing, magnetism, and charge order in the spin-doped attractive Hubbard gas, arXiv:2511.10605 (2025).
- [73] N. Jain, J. Zhang, M. Culemann, and P. M. Preiss, Programmable assembly of ground state fermionic tweezer arrays, arXiv:2512.09849 (2025).
- [74] T. Hammel, M. Kaiser, D. Dux, M. Weidemüller, and S. Jochim, Atom and spin resolved imaging in a single shot, arXiv:2512.09865 (2025).
- [75] O. Abdel Karim, A. Muzi Falconi, R. Panza, W. Liu, and F. Scazza, Single-atom imaging of ^{173}Yb in optical tweezers loaded by a five-beam magneto-optical trap, *Quantum Science and Technology* **10**, 045019 (2025).
- [76] E. Ibarra-García-Padilla, C. Feng, G. Pasqualetti, S. Fölling, R. T. Scalettar, E. Khatami, and K. R. A. Hazzard, Metal-insulator transition and magnetism of SU(3) fermions in the square lattice, *Phys. Rev. A* **108**, 053312 (2023).
- [77] S. Dörscher, R. Schwarz, A. Al-Masoudi, S. Falke, U. Sterr, and C. Lisdat, Lattice-induced photon scattering in an optical lattice clock, *Phys. Rev. A* **97**, 063419 (2018).
- [78] L. Olschewski, Messung der magnetischen Kerndipolmomente an freien ^{43}Ca -, ^{87}Sr -, ^{135}Ba -, ^{137}Ba -, ^{171}Yb - und ^{173}Yb - Atomen mit optischem Pumpen, *Zeitschrift für Physik* **249**, 205 (1972).
- [79] P. Thekkepatt, Digvijay, A. Urech, F. Schreck, and K. van Druuten, Measurement of the g factor of ground-state ^{87}Sr at the parts-per-million level using co-trapped ultracold atoms, *Phys. Rev. Lett.* **135**, 193001 (2025).
- [80] A. Celi, P. Massignan, J. Ruseckas, N. Goldman, I. B. Spielman, G. Juzeliūnas, and M. Lewenstein, Synthetic gauge fields in synthetic dimensions, *Phys. Rev. Lett.* **112**, 043001 (2014).
- [81] T.-W. Zhou, G. Cappellini, D. Tusi, L. Franchi, J. Paravicini, C. Repellin, S. Greschner, M. Inguscio, T. Giamarchi, M. Filippone, J. Catani, and L. Fallani, Observation of universal Hall response in strongly interacting Fermions, *Science* **381**, 427 (2023).
- [82] T. Zhou, T. Beller, G. Masini, J. Parravicini, G. Cappellini, C. Repellin, T. Giamarchi, J. Catani, M. Filippone, and L. Fallani, Measuring hall voltage and hall resistance in an atom-based quantum simulator, *Nature Communications* **16**, 10247 (2025).
- [83] L. Tarruell, D. Greif, T. Uehlinger, G. Jotzu, and T. Esslinger, Creating, moving and merging Dirac points with a Fermi gas in a tunable honeycomb lattice, *Nature* **483**, 302 (2012).
- [84] D. Wei, D. Adler, K. Srakaew, S. Agrawal, P. Weckesser, I. Bloch, and J. Zeiher, Observation of Brane Parity Order in Programmable Optical Lattices, *Phys. Rev. X* **13**, 021042 (2023).
- [85] S. Ma, J. Dolde, X. Zheng, D. Ganapathy, A. Shtov, J. Chen, A. Stöltzel, B. J. Christensen, and S. Kolkowitz, Enhancing optical lattice clock coherence times with erasure conversion, *PRX Quantum* **6**, 040340 (2025).
- [86] T. Plassmann, L. Schaefer, M. Menashes, and G. Salomon, Rapid state-resolved single-atom imaging of alkaline-earth fermions, arXiv:2602.19876 (2026).
- [87] J. Höschele, S. Buob, A. Rubio-Abadal, V. Makhalov, and L. Tarruell, Atom-Number Enhancement by Shielding Atoms From Losses in Strontium Magneto-Optical Traps, *Phys. Rev. Appl.* **19**, 064011 (2023).
- [88] W. H. Richardson, Bayesian-Based Iterative Method of Image Restoration, *J. Opt. Soc. Am.* **62**, 55 (1972).
- [89] M. Cheneau, R. Journet, M. Boffety, F. Goudail, C. Kulcsár, and P. Trouné-Peloux, Fast, accurate, and predictive method for atom detection in site-resolved images of microtrap arrays, *Phys. Rev. Appl.* **24**, 064039 (2025).